Journal of Materials Chemistry A

ROYAL SOCIETY OF CHEMISTRY

COMMUNICATION

View Article Online
View Journal | View Issue

Cite this: J. Mater. Chem. A, 2025, 13, 40655

Received 6th July 2025
Accepted 11th November 2025

DOI: 10.1039/d5ta05452d

rsc.li/materials-a

A phosphite-incorporated crystalline–amorphous cobalt-based electrocatalyst *via* surface-confined chemical reduction for efficient hydrogen evolution reaction

Jean Marie Vianney Nsanzimana, †*[abc] Charles Otieno Ogolla, †*[a] Muhammed Fasil Puthiyaparambath,[d] Nastaran Farahbakhsh, [b] Yilmaz Sakalli, [a] Marco Hepp, [a] Jonas Frohne, [a] Walter Sebastian Scheld, [a] Ranjit Thapa,*[de] Manuela S. Killian [b] and Benjamin Butz [a]

Targeted phase engineering of nanomaterials through non-equilibrium synthesis strategies provides a rich platform for the development and tuning of nanostructured catalysts with outstanding properties and advanced stability. Unconventional phases or even complex heterostructures play a crucial role in the performance of catalysts for efficient water electrolysis. By utilizing a controlled, iterative reduction synthesis route, a tailored binder-free cobalt boride-phosphite electrode (Co_xB-[0.2]P–O) with mixed crystalline–amorphous phases is developed. The tailored cobalt boride chemistry by phosphites enables the alteration of the d electron distribution of cobalt, bringing the H* adsorption energy into the optimal range and thereby enhancing the HER activity. Comprehensive microstructure and spectroscopic analyses proved the success of the one-pot strategy to modulate the microenvironment chemistry of cobalt by incorporating boron and phosphite. Moreover, the tailored formation of nanostructures with locally varying morphology by the co-existence of amorphous and crystalline phases on the nanometer scale is confirmed. This approach facilitates the rational design for tuning the metal boride-based catalysts' activity for hydrogen evolution by tailored chemistry of the metal active centers and thus the phase engineering of similar nanomaterials while avoiding the necessity of any thermal post-treatment processes.

1 Introduction

Electrochemical energy technologies will significantly contribute to the transition to a sustainable and carbon-neutral economy in order to decarbonize the energy sector.[1] One of the most critical scientific and technological problems is the development of a sustainable and cost-effective water splitting process for industrial-scale production of green hydrogen (H_2) to facilitate the energy transition.[2] Heterogeneous catalysis is a key element of the solution.[3] Benchmark electrocatalysts with a zero hydrogen evolution reaction (HER) overpotential used in low-temperature water electrolysis systems are, however, based on scarce, expensive noble metals (specifically platinum group metal (PGM) catalysts).[4] This makes them economically less attractive and does not meet the requirements for the global demand for green H_2. Consequently, the development of low-cost, stable, and highly efficient hydrogen-evolving materials is of key importance to meet this demand. Earth-abundant transition metal (TM)-based materials have attracted much attention as alternative electrocatalysts, especially in alkaline electrolytes.[5,6] However, chemical modulation strategies of catalysts and economically viable synthesis routes to generate nanostructured materials with durable and enhanced catalytic performances are still required for clean H_2 production, especially at an industrial scale.[4,7]

A major process bottleneck, when operating in alkaline media, is the reduced kinetics due to the water-dissociation energy barrier.[8] However, alkaline water electrolysis allows the utilization of TM-based materials, which serve as PGM-free alternatives with better HER kinetics.[9] Emerging technologies such as anion-exchange membrane water electrolysis (AEMWE), for industrial scale water splitting, increasingly require electrocatalysts that are capable of even operating under mild alkaline conditions (less than or equal to 1 M KOH) or pure water where performance is dependent on the water/oxygen transportation and the stability of the materials at the interfaces.[10,11] In this application context, a rationale for the development of stable membrane and PGM-free electrocatalysts for the HER and water oxidation is paramount.[12,13] To enhance the kinetics of the reduction reaction, the chemical environment of TM-based catalysts can be tailored by incorporating nonmetals and metalloid elements such as phosphorus, sulfur, nitrogen,

[a]Micro- and Nanoanalytics Group, University of Siegen, Paul-Bonatz-Straße 9-11, 57076, Germany. E-mail: jean.nsanzimana@uni-siegen.de; charles.ogolla@uni-siegen.de

[b]Chemistry and Structures of Novel Materials, University of Siegen, Paul-Bonatz-Straße 9-11, 57076 Siegen, Germany

[c]Department of Industrial Engineering, University of Padova, Via Marzolo 9, 35131 Padova (PD), Italy

[d]Department of Physics, SRM University-AP, Amaravati, Andhra Pradesh 522240, India. E-mail: ranjit.t@srmap.edu.in

[e]Centre for Computational and Integrative Sciences, SRM University-AP, Andhra Pradesh 522240, India

† These authors contributed equally to this work.

selenium, and boron.[14,15] Engineering of the material's morphology, crystal structure, and catalyst support is leveraged to improve the extrinsic catalytic activity of complete electrodes.[3] A careful choice of the substrate material and the design of the substrate/catalyst interface, especially for highly conductive substrates, is also important.[16] This enables strong adhesion and enhanced charge transfer due to extended exposure of more catalytic active sites to adsorbates promoting the HER activity and life-cycle of the electrocatalysts.[17] By combining the above strategies, earth-abundant transition metal-based catalysts are developed with high activity comparable to precious metal-based catalysts.

TM-based borides and boron oxides, which are abundant and provide economically attractive alternatives, show promising catalytic performance for water splitting.[18–21] Central to this class of materials is cobalt boride with moderate HER activity.[22] Cobalt boride (Co_xB)-based materials take advantage of the fact that Co as a first-row transition metal possesses three unoccupied d-orbitals facilitating facile surface chemical interactions.[23] Metalloids such as boron and phosphorus and their oxidized forms, such as borates and phosphates, have been known to influence the electronic configuration of the metal sites.[24,25] Despite the considerable progress made in the development of efficient cobalt boride-based electrocatalysts, advanced synthesis strategies affording tailored cobalt chemistry, modulation of the electronic nature of cobalt and advanced phase engineering at the nanoscale for the HER are crucial.[26]

Besides the careful choice of a performant material system, the global and, more importantly, local crystal structure of the chosen system plays a significant role in determining its catalytic performance.[27] Amorphous systems inherently possess dangling bonds randomly oriented in space, which results in a higher degree of unsaturated electronic configurations.[28] Consequently, purely amorphous catalysts possess a large fraction of unsaturated active sites facilitating efficient adsorption and surface reactions at the cost of conductivity.[27,28] In contrast, crystalline phases enhance the material's intrinsic conductivity.[27,29] It is therefore necessary to produce catalysts that take advantage of the synergistic effect of complex heterostructures consisting of crystalline and amorphous phases at the nanoscale.[26,27,30] TM-boride catalysts are typically synthesized *via* chemical reduction reactions of transition metal cations in aqueous solution using alkali metal tetrahydrides as reducing agents and a boron source to precipitate metal-borides.[31–33] However, this reaction is spontaneous and it is a challenge to control the final products. Such products are mostly amorphous,[34,35] and typically require post-thermal treatment to induce some form of crystallinity or utilize highly conductive carbon to enhance the electrocatalytic performance.[22,36] TM-boride-based nanomaterials, therefore, provide a suitable platform for phase engineering at the nanoscale to develop efficient HER electrocatalysts with unique chemistry, morphology, and unconventional mixed crystalline–amorphous phases using only a facile and cost-effective wet-chemical reduction process.[37]

Herein, we use an elaborate synthesis strategy to develop a series of self-supported, amorphous–crystalline (heterostructured), nanostructured cobalt boride phosphite electrocatalysts. Our synthesis technique avoids any additional energy-intensive annealing process as commonly employed to induce crystallinity in TM-boride based catalysts synthesized in an aqueous reducing solution. Comprehensive electrochemical and structural characterization of Co_xB–O (–O denoting the presence of oxygenated species, *i.e.*, Co–O, B–O), reference $Co(OH)_2$ as well as the complex, highly performing Co_xB-[0.2]P–O samples, revealed that the enhanced catalytic activity resulted from the unique heterostructure and synergistic effects of cobalt with boron and phosphite, as further revealed by the theoretical calculations.

2 Results and discussion

2.1. Fabrication and surface chemistry analysis of the self-supported electrode

The electroless preparation of a series of self-supported hierarchical cobalt boride-based electrodes is schematically shown in Fig. 1A–H (details in Fig. S1). Highly open-porous and hollow

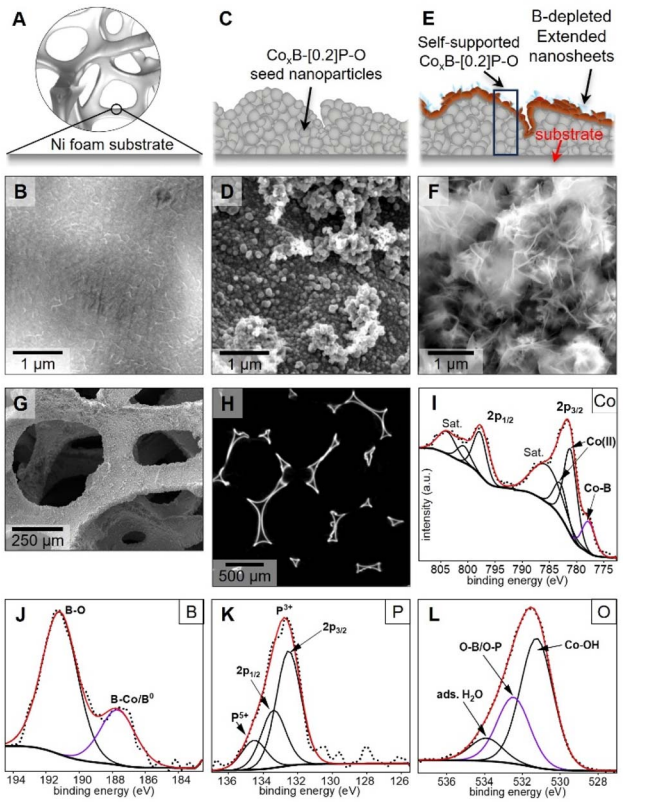

Fig. 1 (A–G) Electrode fabrication depicted by schematics plus representative SEM images: synthesis stages starting from a clean NF surface (A and B) through intermediate steps (C and D: seed nanoparticle formation) to the final product (E and F: final Co_xB-[0.2]P–O catalyst with typical $Co(OH)_2$ nanosheets), (G) SEM overview of the high-performing electrode demonstrating complete coverage and good adhesion, (H) ortho-slice (cross-section) of 3D reconstruction from μCT of hollow NF, (I–L) XPS spectra of Co, B, P, and O.

nickel foam (NF) (Fig. 1G, H and S2A) is used as the substrate as it allows for excellent liquid/gas transport, is chemically stable, provides high electrical conductivity and a suited surface for the catalyst fabrication/operation.[38] X-ray micro-tomography (μCT) furthermore depicts the hollow nature and thus material-saving NF due to the thin walls of the foam struts (Fig. 1H). The facile synthesis employs an iteratively controlled chemical reduction reaction of cobalt cations (solution A: $Co(NO_3)_2 \cdot 6H_2O$) by mixtures of reducing agents in an aqueous solution (solution B: $NaBH_4$ and $Na_2HPO_3 \cdot 5H_2O$). Sodium borohydride acts as a strong reaction-controlling reducing agent, while sodium phosphite is a weaker reducing agent.

This combination of reducing agents facilitates, both, the inherent formation of severe aggregated nanoparticles and immediate doping by phosphite, while at a later stage, the complex amorphous–crystalline cobalt boride phosphite (Co_xB-[0.2]P–O, where –O refers to the presence of corresponding oxidized species, *i.e.*, Co–O and P/B–O due to the repetitive exposure to air during synthesis and post-synthesis) catalyst is formed. The cobalt source, *i.e.*, solution A, is first adsorbed on the NF substrate (Fig. S1) and subsequently immersed in the reducing solution B. This iterative process was repeated 5 times, whereby the cobalt ions are locally reduced on the surface.[39] As a result, a dense and well-adhering seed nanoparticles on the NF is generated (intermediate state depicted in Fig. 1C, D and S3A) to assure mechanical long-term stability during catalyst operation (Fig. S4), good electron transport and an enhanced surface area (*cf.* Fig. 1B and D). In the last synthesis step, the seed nanoparticle-coated NF substrate is immersed into solution A, while solution B is slowly added. In this reactive mixture, the final catalyst is comprised of embedded seed nanoparticles with extended nanosheets (Fig. 1F, *cf.* Fig. 1D and S2C, D and S3B details in the SI). SEM-EDX analysis demonstrated the presence of Co, B, P, and O, indicating the formation of Co_xB-[0.2]P–O (Fig. S5). In particular, the P content increased in the aged sample due to the inclusion of phosphites. The high energy impact of the rapid exothermic reaction on the roughened seed nanoparticle surface allows for the localized atomic-scale structural rearrangement and thus the formation of amorphous–crystalline heterostructured Co_xB-[0.2]P–O without any additional thermal treatment.

Surface-sensitive X-ray photoelectron spectroscopy (XPS) in Fig. 1I–L confirms the successful incorporation of the B and P species and their impact on the electronic environment of the Co active sites within the catalyst. XPS survey revealed a surface composition of 23.17 at%, 29.71 at%, 29.73 at%, 5.02 at%, and 12.37 at% for B, C, O, P, and Co, respectively (*cf.* Fig. S6). Deconvolution of the Co $2p_{3/2}$ spectrum clearly reveals the tailored Co–B interaction, resulting in a distinct sub-peak at 777.7 eV, which is 0.4 eV shifted to lower binding energy compared to metallic Co^0 (778.1 eV (ref. 40)) due to the electron transfer from boron to cobalt (Fig. 1I).[31,41,42] In addition, there are two major peaks of Co $2p_{3/2}$ at 781.6 eV and Co $2p_{1/2}$ at 797.4 eV, respectively, with a spin–orbit splitting of ΔE = 15.8 eV. Detailed analysis of the Co $2p_{3/2}$ peak reveals two contributions with typical shifts to higher binding energies (781.1 eV and 782.9 eV) owing to cobalt(II) cations bound to highly electro-negative species such as hydroxides and phosphites, respectively.[22,43] The electron transfer between Co and B is further indicated by the positive 0.6 eV shift relative to B^0 (187.1 eV) in the B 1s peak (187.7 eV), attributed to the boride species (Fig. 1J).[36,42,44] Phosphite incorporation into the Co–B system was evidenced by the deconvoluted P 2p spectrum (Fig. 1K) into two major sub-peaks at 133.6 eV and 134 eV (Δ = 0.87 eV) characteristic of the presence of phosphorus(III) species and an extra peak at higher energy for phosphorus(V) in oxidized P–O species.[45,46] Like boron, the phosphorus inclusion into the Co–B system directly modulates the electron density around cobalt atoms, which impacts electron transfer and the hydrogen interaction with the active sites.[47] The O 1s spectrum (Fig. 1L) shows three sub-peaks at 531.5 eV, 532.5 eV, and 533.9 eV. The signals at 531.5 eV and 532.5 eV consistently reveal the presence of mixed metal-oxide/hydroxide (*e.g.* $Co(OH)_2$/CoO) and the P/B–O (in oxidized P species and B–O in boron-oxo species), respectively.[48]

2.2. Microstructural and chemical characterization

A comprehensive scale-bridging investigation of the microstructure, crystal structure and chemistry of the electrodes with emphasis on the final catalyst is indispensable to understand catalyst functionality, performance and long-term stability. The continuous coating of the NF surface is confirmed by SEM top-view and cross-sectional imaging (Fig. 1F, G, 2A and B) as corroborated by the Co mapping. The coating roughness (Fig. 2B), governed by the seed nanoparticles with a mean grain size of the polycrystalline Co_xB-[0.2]P–O of around 100 nm (Fig. 2G), enhances the active surface area and thus promotes the HER. The tailored two-step reduction reaction resulted in the formation of the targeted hierarchical Co_xB-[0.2]P–O catalyst, with the surface exposed exhibiting amorphous–crystalline morphology, surpassing conventional reduction strategies with a typical amorphous structure.[22]

The high-angle annular dark-field scanning TEM (HAADF-STEM) and the corresponding X-ray spectroscopy (TEM-EDX) confirmed the successful synthesis of cobalt-boride with phosphorus in phosphite homogeneously incorporated (Fig. 2C, D, and S10). Fig. 2B and E demonstrate the continuous coverage of the Co_xB-[0.2]P–O catalyst with seed nanoparticles generated during the coating step and an amorphous–crystalline heterostructure (Fig. 2F–H and S8). Fig. 2F details the morphology of the amorphous–crystalline Co_xB-[0.2]P–O at the catalyst surface with crystalline domains of around 10 nm embedded in the amorphous matrix (Fig. 2G and H). The nanocrystalline nature of the Co_xB-[0.2]P–O particles is reflected as severe peak broadening in XRD (Fig. S7). The complex architecture of the developed electrocatalyst is further confirmed by three-dimensional (3D) tomographic reconstruction (Fig. S13). The reconstruction delineates the nanostructures showing agglomerated nanoparticles (seed nanoparticles) at the bottom of the electrode covered by porous nanosheets at the top exposing a large surface area. This hierarchical morphology is necessary for efficient mass transport during the catalytic reaction with

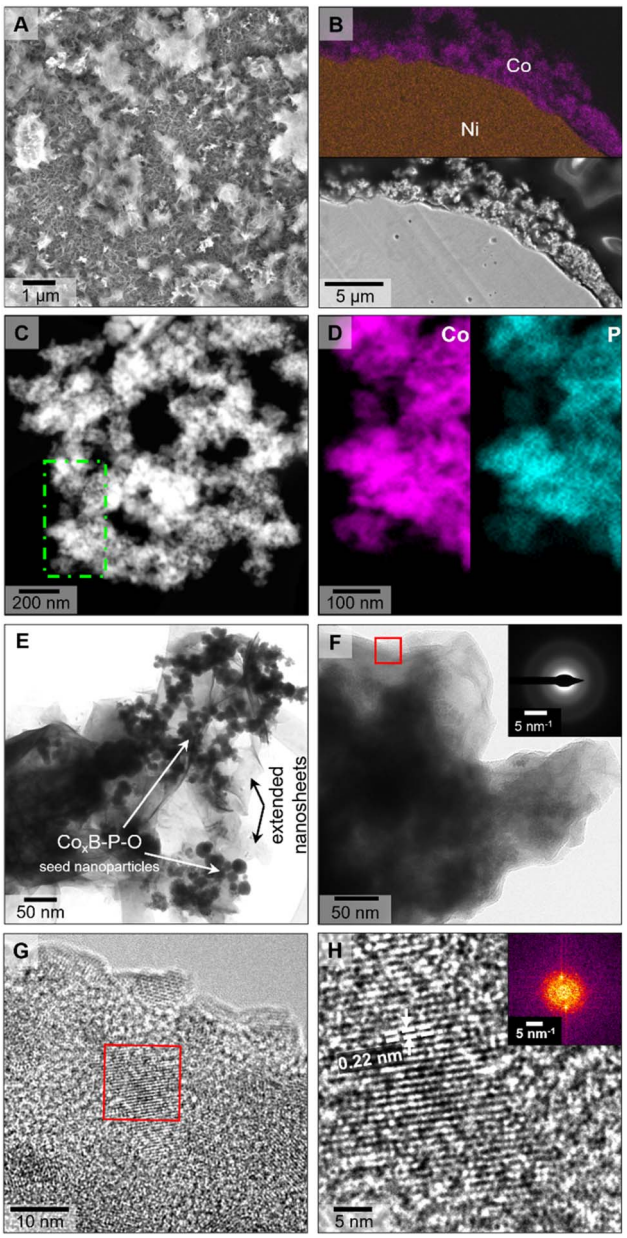

Fig. 2 Morphology and microstructure of catalyst regions: (A) top-view SEM overview and (B) cross-sectional SEM micrograph of the electrode with corresponding EDXS elemental maps of Ni and Co, (C) high-angle annular dark-field scanning TEM (HAADF-STEM) image of the scratched sample with the region where EDX maps in (D) were collected indicated (green box), (D) STEM-energy dispersive X-ray spectroscopy (STEM-EDXS) elemental maps of Co and P from (C), (E) bright-field TEM micrograph of the exposed electrode surface (scratched sample) showing Co_xB-[0.2]P–O seed nanoparticles with extended B-depleted nanosheets, (F) region showing the on-grown amorphous–crystalline catalyst heterostructure, (G) HRTEM micrograph of the amorphous–crystalline Co_xB-[0.2]P–O heterostructure from (F), (H) HRTEM image showing lattice fringes from the region marked red in (G) (the inset is the FFT of the region shown in (H)).

the large surface area providing a large number of active sites for surface chemical reactions.[49]

Cross-sectional TEM samples, prepared by ultramicrotomy, enabled the detailed characterization of the local composition and bonding by STEM electron energy loss spectroscopy (EELS) (Fig. 3). In Fig. 3A, D, and G, both the seed nanoparticles and the final catalyst region are differentiated. The dense Co_xB-[0.2]P–O particles with the final catalyst coating appear bright in the HAADF-STEM images in contrast to the faint nanosheets (Fig. 3A and D). The systematic co-occurrence of B, Co, and a minor concentration of O, as depicted in Fig. 3B, E, and H, proves the successful formation of cobalt boride (Co_xB-[0.2]P–O). In contrast, the nanosheets (upper dataset) consist of Co, higher O concentration and reduced B concentration. Both Co_xB-[0.2]P–O as well as the nanosheets are linked to specific Co species (*cf.* Fig. 3C, F, I, S11 and S12). Owing to the low local concentration and the unsuited shape of the ionization edge in conjunction with the challenging sample geometry, any P distribution could not be derived with the EELS technique (see the experimental section). However, the homogeneous incorporation of P is proven by STEM X-ray spectroscopy (Fig. 2D and S10) and XPS (Fig. 1K and S6).

Furthermore, EELS allows for the separation of the Co oxidation state as particularly the L_3 intensity (in correlation with the L_2 intensity) directly correlates with the number of unoccupied 3d states and is thus a measure of the change in Co oxidation state. The seed nanoparticles and final catalyst material show a higher, but mixed oxidation state of Co (Fig. 3C, F, and I) in comparison to the nanosheets. The higher mean oxidation state is not necessarily reflected in an increased L_3/L_2 ratio of the respective peak heights but in a significantly broader L_3 peak (and thus intensity).

Both the $L_{3,2}$ peak maxima/onsets of the Co_xB-[0.2]P–O (seed nanoparticles + final catalyst) are systematically shifted towards higher binding energies by approximately 1 eV compared to the hydroxide reference, indicating partial electron transfer to highly electro-negative adjacent species like B and P.[50] While the peak shape of the nanosheets is similar to that of the Co hydroxide reference with a periodic atomic arrangement, the significantly broadened Co L_3 peak of the catalyst indicates strong local variations of the composition and next-neighbor configuration (particularly B/P/O(H)) on the atomic scale and thus varying electronic environments of the active Co species. This is indicative of a change in the ligand field of the active Co catalyst centers. The incorporation of B and P (as phosphite) creates a unique ligand environment around Co, which leverages the electron-withdrawing and electron-donating properties of both species. While B may withdraw or donate (reverse electron transfer) electron density from Co, depending on whether the material is crystalline or amorphous, P donates electron density resulting in a complementary interaction with a balanced electronic environment and tailored ligand field, thereby optimizing the overall ad/de-sorption of reactants and facilitating enhanced HER catalytic activity as reflected in the catalytic HER performance.

2.3. Electrochemical performance

The electrocatalytic activity of the electrodes for the HER was studied in a common three-electrode cell containing 1.0 M $KOH_{(aq)}$ electrolyte. Graphite and mercury oxide/mercury (HgO/

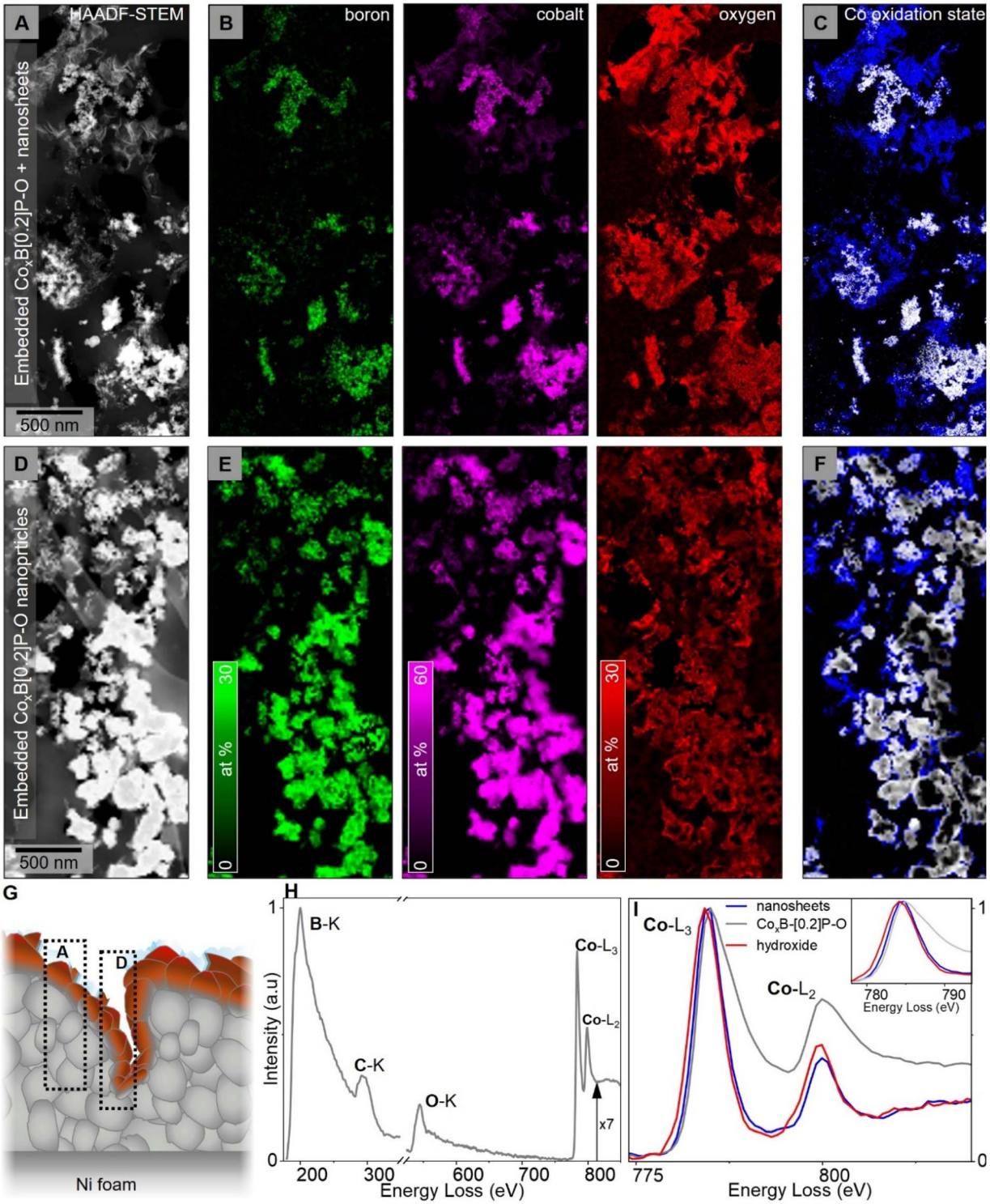

Fig. 3 Comprehensive EELS analyses of (A–C) the final catalyst on (D–F) seed nanoparticles with (G) indicative positions within the electrode: (A and D) high-angle annular dark-field scanning TEM (HAADF-STEM) images showing bright seed nanoparticles and final catalyst (high density) in contrast to intermediate gray nanosheets (lower density and lower projected thickness), (B and E) corresponding B, Co, and O elemental maps (in at% with P and H concentration omitted due to instrumental and methodological limitations); and (C and F), Co oxidation-state maps (colors blue and grey correspond to line colors in (I): Co-$L_{2,3}$ spectra), (H) overview EEL spectrum, (I) representative cobalt $L_{2,3}$ spectra of the final catalyst region and nanosheet regions compared to as-synthesized $Co(OH)_2$ reference with shifts in Co L_3 edge as the inset.

Hg) were used as counter current and reference electrodes, respectively (details in the SI: electrochemical evaluation section). The HER properties of the Co_xB-[0.2]P–O catalyst coating were determined from comparative *iR*-corrected linear sweep voltammetry (LSV) curves. The LSV curve of Co_xB-[0.2]P–O shows a significant shift toward lower potentials compared to

that of both the NF substrate and even a commercial 20% Pt/C catalyst loaded on the NF (Fig. 4A). The enhanced catalytic performance of the self-supported Co_xB-[0.2]P–O electrodes is characterized by a very low overpotential of 33 mV (Fig. 4B and S14) at the standard geometric current density (η @ 10 mA cm^{-2}). It shows promising electrocatalytic performance compared to reported self-supported cobalt-based catalysts (Table S1). The control samples, Co_xB–O, ($Co(OH)_2$), and the NF substrate required relatively higher potential values (103 mV for Co_xB–O, 208 mV for $Co(OH)_2$ and 306 mV for NF at η @ 10 mA cm^{-2}). In contrast to powder catalysts such as Pt/C catalyst and the bare NF substrate, this self-supported catalyst overcomes the use of binders, such as Nafion, to stabilize the catalyst, and synergistically with the substrate, enables improved mass transport, enhanced access to active sites, less interfacial resistance, and higher electrical conductivity.

The mechanism of the HER in an alkaline solution involves an additional step of breaking water molecules to generate protons.[51] This process, therefore, requires extra energy for successful water splitting and causes more sluggish reaction kinetics.[52] This is depicted by the Tafel value for the optimized Co_xB-[0.2]P–O which was observed to be the lowest among the investigated sample series at 49 mV dec^{-1}, which is competitive to Pt/C (35 mV dec^{-1}) (Fig. 4B). Such a low value infers an enhanced electron-coupled water dissociation step, known to be the rate-determining step for the HER under alkaline conditions.[22] This demonstrates that our boron and phosphite-incorporated catalyst (Co_xB-[0.2]P–O) has more efficient HER kinetics relative to $Co(OH)_2$ and Co_xB–O counterparts. These enhanced reaction kinetics are corroborated by detailed analyses of Nyquist plots retrieved from electrochemical impedance spectroscopy (EIS) measurements (Fig. 4C). The charge transfer resistance (R_{ct}) values, determined from the radii of the Nyquist plots, were 4.1 Ω, 17.6 Ω, and 69.4 Ω for Co_xB-[0.2]P–O, Co_xB–O (control catalyst), and $Co(OH)_2$ (control catalyst), respectively. Evidently, the optimized boron and phosphite-doped catalyst has a reduced R_{ct} value compared to the counter and control electrocatalysts.

This comparison proves a better adsorption–desorption efficiency of the reactants due to better charge transfer by the reduced binding energy due to the P-containing phosphite co-doping.[24] The control catalyst $Co(OH)_2$ exhibits the highest R_{ct} value most likely since this material did not include cobalt-boride or phosphite in the structure. The electronic configuration of cobalt determined by XPS analysis showed that the presence of both B and P of phosphite ensured the tailored chemistry of Co through charge transfer processes,[53] and as a consequence the observed better charge transfer in Co_xB-[0.2]P–O. Among the series of catalysts, only the $Co(OH)_2$ control catalyst exhibits a purely crystalline form (Fig. S8 and S9), whereas both Co_xB-[0.2]P–O and Co_xB–O show mixed amorphous–crystalline heterostructures. We therefore conclude that the modulated chemistry of cobalt by boron and phosphite incorporation as well as the co-existence of mixed phases causes the synergistic enhancement of the electron transfer process.

The Co_xB-[0.2]P–O electrocatalyst exhibits by far the highest hydrogen production per active site as demonstrated by a superior TOF value of 0.87 s^{-1} at a voltage of −0.05 V *vs.* RHE, which is approximately 15 times higher than that of the counter catalyst (Co_xB–O) (Fig. 4D and S15). As anticipated from the hierarchical and rough morphology of the catalyst surface, these electrocatalysts showed relatively similar electrocatalytic surface area (ECSA) which correlates with the double layer capacitance (C_{dl}) values of Co_xB-[0.2]P–O (3.5 mF cm^{-2}), Co_xB–O (3.1 mF cm^{-2}), and $Co(OH)_2$ (2.6 mF cm^{-2}) (Fig. 4E and S16). Consistently, Co_xB-[0.2]P–O shows better HER performance compared to Co_xB–O and the $Co(OH)_2$ counterparts in Fig. 4F, where the ECSA-normalized activity is shown. While the ECSA values of the three materials are similar, the TOF measurements provide evidence that the local chemistry of the active site plays a more significant role in promoting the electrocatalytic efficiency of these catalysts.

The Co_xB-[0.2]P–O electrodes show promising long-term stability after 1000 CV cycles even under alkaline operation conditions as demonstrated by well-overlapping LSV curves before

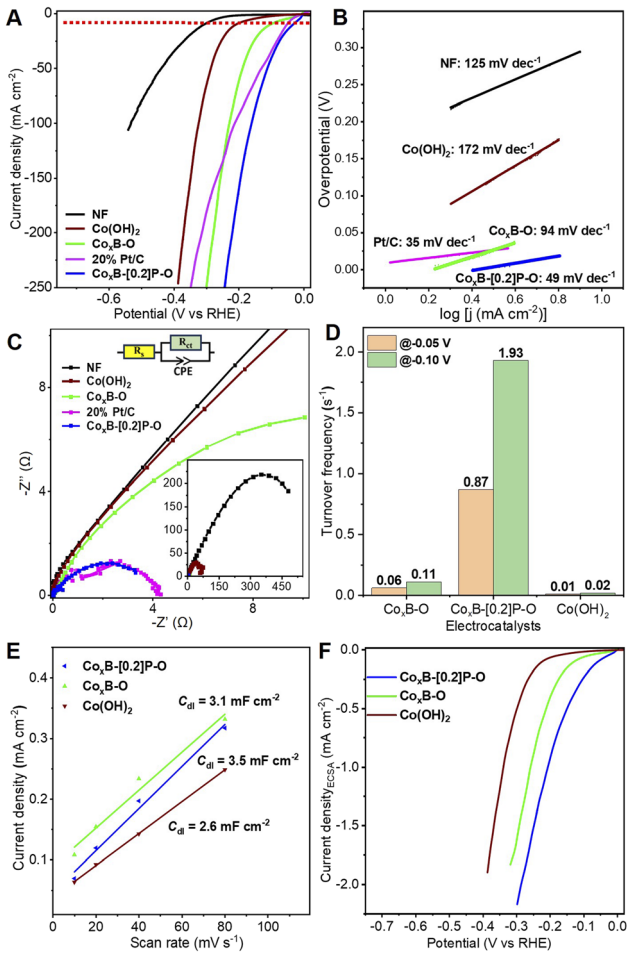

Fig. 4 Electrocatalytic performance of catalysts for the HER: (A) LSV curves for as-fabricated catalysts Co_xB-[0.2]P–O, Co_xB–O, $Co(OH)_2$, commercial Pt/C, and bare NF in 1.0 M KOH, (B) Tafel slopes and (C) EIS Nyquist plots of Co_xB-[0.2]P–O, Co_xB–O, $Co(OH)_2$, commercial Pt/C, and bare NF; insets show the equivalent circuit used for fitting the data and overall Nyquist plot as an overview, (D) bar graph of the turnover frequency (TOF), (E) double-layer capacitance, (F) ECSA normalized LSV of Co_xB–O, Co_xB-[0.2]P–O, and $Co(OH)_2$.

and after cycling (Fig. 5A). Furthermore, the R_{ct} values remain unchanged (inset in Fig. 5A). Complementary to this performance, the chronopotentiometric curve exhibits no noticeable increases in overpotentials in the tested period (Fig. S17).

Post-operation SEM micrographs further confirm the preservation of the original morphology with only slightly thickened nanosheets (*cf.* Fig. 1B, C, B–D and S4) corroborating the excellent mechanical stability during operation. Post-operation TEM analysis (Fig. 5E–H and S18) also confirms the sustained coexistence of amorphous regions and nanocrystalline domains even after 1000 CV cycles further attesting to the structural robustness of the catalyst. Combined SEM and TEM analyses of this electrode after stability testing demonstrate minimal degradation as the self-support configuration on the metal foam prevents delamination as typically observed in powder-based catalysts during operation,[54] with the open-porous nickel foam (NF) facilitating efficient mass transport. The strong anchorage of the catalyst even after the stability test on the highly porous and conductive 3D metal substrates provides a major advantage in contrast to conventional drop-cast coatings.[55,56]

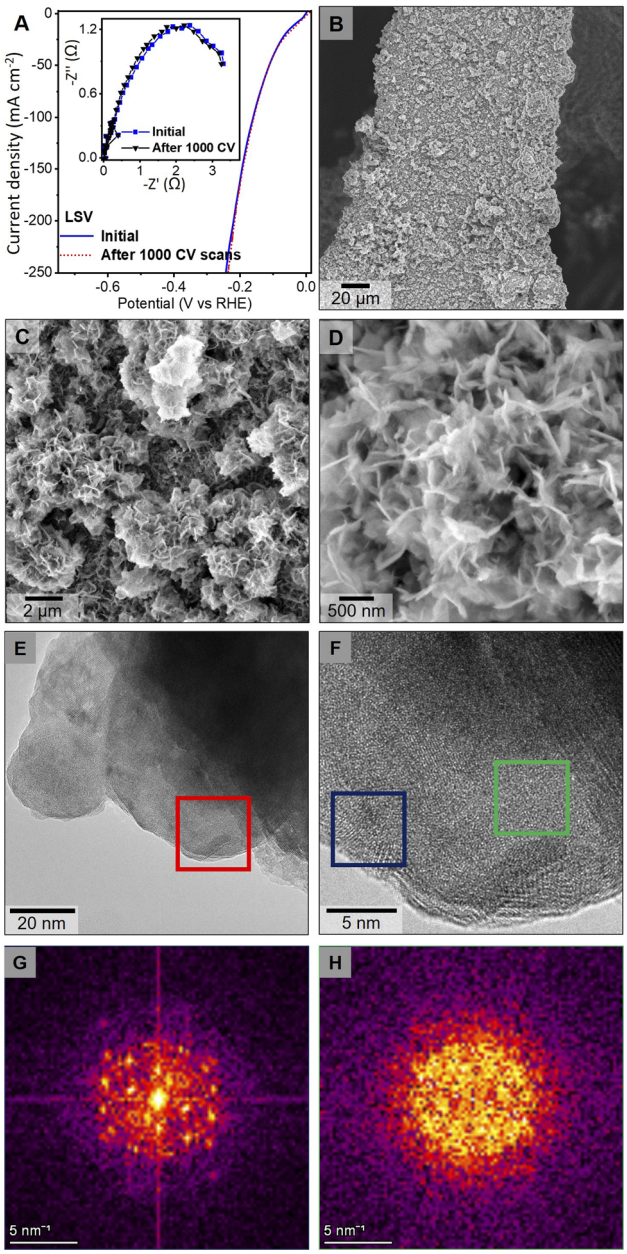

Fig. 5 Stability characterization: (A) LSV curves before and after 1000 CV scans for the optimized Co_xB-[0.2]P–O catalyst (the inset in (A) shows overview Nyquist plots), (B–D) SEM images of the electrode after 1000 CV scans, (E and F) HRTEM images highlighting representative amorphous–crystalline regions, (G and H) corresponding FFT patterns from the blue and green boxed areas in (F) revealing retained crystalline (G) and amorphous (H) regions.

2.4. Theoretical characterization

Density functional theory (DFT) calculations were performed to investigate the role of phosphite in Co_xB–O (CoB–O system) and to elucidate the HER active sites using Vienna *Ab initio* Simulation Package (VASP).[57] The phosphites and the O atoms due to the oxidized species were preferentially adsorbed on the (001) surface termination of CoB (CoB–O–P system). The optimized configurations of CoB–O and CoB–P–O systems are shown in Fig. 6A and B. The Gibbs free energy of hydrogen (ΔG_{H^*}) is a widely accepted descriptor for evaluating the catalytic performance toward the HER.[58] In general, a ΔG_{H^*} value close to zero indicates the optimal HER activity, thereby achieving high HER activity.

The catalytic efficiency of CoB–O and CoB–P–O was evaluated by calculating ΔG_{H^*} for hydrogen atoms at both Co and B active sites. The free energy profile in Fig. 6C reveals that for CoB–O, the ΔG_{H^*} values are −0.52 eV for the B site and −0.12 eV at the Co site. In contrast, the corresponding values for CoB–P–O are −0.34 eV at

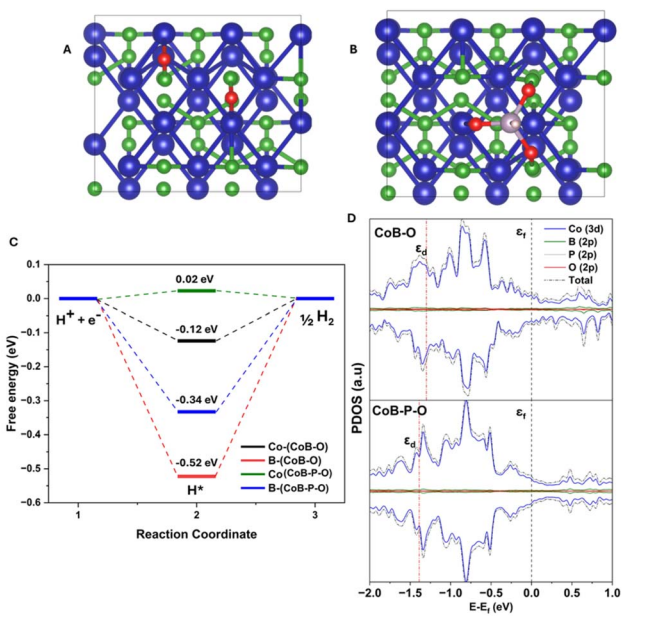

Fig. 6 (A) Optimized configurations of the CoB–O system and (B) CoB–P–O system; colour codes: violet, green, red and grey represent Co, B, O and P, respectively. (C) Calculated free energy profile of CoB–O and CoB–P–O systems, and (D) PDOS of CoB–O and CoB–P–O (Fermi energy levels (ε_f) and d-band center (ε_d) are marked by black and red dashed lines).

the B site and 0.02 eV at the Co site, with the latter being much closer to zero and substantially improved activity compared to CoB–O. These results indicate that phosphite incorporation enables more optimal H* adsorption at the Co site, thereby balancing the adsorption–desorption energetics and enhancing the HER activity.

To elucidate the origin of the enhanced activity, electronic structure analyses were performed, as shown in Fig. 6D. The projected density of states (PDOS) of CoB–O and CoB–P–O systems confirms a non-zero occupation at the Fermi level, which reflects the metallic nature of the catalysts, which is favourable for electron transfer during the electrocatalytic process. Bader charge analysis reveals that upon incorporation of phosphite, approximately $0.97e^-$ are transferred from phosphite to the system, thereby altering the d electron distribution of Co. Consequently, the d-band center (ε_d) of Co shifts below the Fermi level, leading to a redistribution of unoccupied states and a weakening of H* adsorption, which is reflected in the positive value of ΔG_{H*}.[59] This is also validated by the increase in the bond length of Co–B from 2.13 Å to 2.28 Å upon phosphite incorporation, which can be attributed to the electron accumulation around the Co centre. The enhanced electron density weakens the Co–B interaction, resulting in bond elongation and subsequently affecting the electronic structure and adsorption properties. Thus, the incorporation of phosphite modifies the electronic structure of Co–B, bringing the H* adsorption energy into the optimal range and thereby enhancing the HER activity.

3 Conclusions

A facile, cost and resource-effective method has been developed to prepare a self-supported, highly efficient and long-term stable Pt-like Co_xB-[0.2]P–O electrocatalyst for the HER. A comprehensive scale-bridging investigation of the microstructure and chemistry of the complete electrode with emphasis on the final catalyst material has been employed to explain the enhanced electrocatalytic and Pt-competitive HER performance of the electrode in comparison to previous Co_xB based catalysts. Its superior performance is attributed to the complex heterostructure morphology with co-existing crystalline and amorphous phases. Additionally, the modulation of the Co active site chemistry and ligand field due to the incorporation of both boron and phosphite promotes catalytic activity and reduces charge transfer resistance. In the CoB–P–O system, phosphite incorporation reduces the ΔG_{H*} at both Co and B sites (to 0.02 eV and −0.34 eV, respectively) compared to the CoB–O system, indicating more favorable HER kinetics. DFT calculations further show that this effect arises from phosphite-induced modulation of Co electronic states near the Fermi level, making Co_xB–P–O a more promising catalyst than Co_xB–O. The comprehensive investigation unravelled the complex interplay between morphology, crystal structure, chemistry and bonding required for the successful production of highly efficient electrocatalysts. This work demonstrated a quite simple synthesis strategy and facilitates the development of more complex earth-abundant transition metal electrocatalysts with high activity toward electrochemical reactions for water splitting.

Author contributions

JMVN: project administration, conceptualization, experimental design, project management, material synthesis, physicochemical/electrochemical characterization and analysis, data interpretation, manuscript writing, editing and revision; COO: experimental design, TEM investigation, sample preparation, data analysis and interpretation, manuscript writing, editing and revision; JF: STEM tomography and μCT, 3D visualization; MH: SEM-EDXS; NF: XPS; YS and WSS: assisted in material characterization; MFP and RT: theorical experiment and manuscript editing and revision; MK: project supervision, project administration, data interpretation, manuscript writing, review and editing; BB: project supervision, project administration, data interpretation, manuscript writing, editing and revision.

Conflicts of interest

There are no conflicts to declare.

Data availability

The data that support the findings in this study are available from the corresponding authors upon reasonable request.

Acknowledgements

This project has received funding from the European Union's Horizon 2020 research and innovation program under the Marie Skłodowska-Curie grant agreement No. 945422. Part of the study was performed at the DFG-funded Micro-and Nano-analytics Facility (MNaF) of the University of Siegen (INST 221/131-1) by utilizing its major instrumentation (FEI Talos F200X TEM: DFG INST 221/93-1, DFG INST 221/126-1). This project has received funding from the European Union's Horizon 2020 research and innovation program under the Marie Skłodowska-Curie grant agreement No. 101102946. The authors thank the National Supercomputing Mission (NSM) for access to PARAM Rudra for providing central computational facilities. M. F. P. and R. T. acknowledge ASEAN India Collaborative Research for the funding support CRD/2024/000716.

Notes and references

1 M. Chatenet, B. G. Pollet, D. R. Dekel, F. Dionigi, J. Deseure, P. Millet, R. D. Braatz, M. Z. Bazant, M. Eikerling, I. Staffell, P. Balcombe, Y. Shao-Horn and H. Schäfer, *Chem. Soc. Rev.*, 2022, **51**, 4583–4762.
2 T. Terlouw, L. Rosa, C. Bauer and R. McKenna, *Nat. Commun.*, 2024, **15**, 7043.
3 Z. W. Seh, J. Kibsgaard, C. F. Dickens, I. Chorkendorff, J. K. Nørskov and T. F. Jaramillo, *Science*, 2017, 355.
4 Y. Aykut and A. Bayrakçeken Yurtcan, *Electrochim. Acta*, 2023, **471**, 143335.

5 M. N. Lakhan, A. Hanan, A. Hussain, I. Ali Soomro, Y. Wang, M. Ahmed, U. Aftab, H. Sun and H. Arandiyan, *Chem. Commun.*, 2024, **60**, 5104–5135.
6 U. Shahzad, M. Saeed, H. M. Marwani, J. Y. Al-Humaidi, S. U. Rehman, R. H. Althomali and M. M. Rahman, *Int. J. Hydrogen Energy*, 2024, **65**, 215–224.
7 Z. Zou, K. Dastafkan, Y. Shao, C. Zhao and Q. Wang, *Int. J. Hydrogen Energy*, 2024, **51**, 667–684.
8 N. Mahmood, Y. Yao, J.-W. Zhang, L. Pan, X. Zhang and J.-J. Zou, *Adv. Sci.*, 2018, **5**, 1700464.
9 A. A. Feidenhans'l, Y. N. Regmi, C. Wei, D. Xia, J. Kibsgaard and L. A. King, *Chem. Rev.*, 2024, **124**, 5617–5667.
10 N. Du, C. Roy, R. Peach, M. Turnbull, S. Thiele and C. Bock, *Chem. Rev.*, 2022, **122**, 11830–11895.
11 F. Moradi Nafchi, E. Afshari and E. Baniasadi, *Int. J. Hydrogen Energy*, 2024, **52**, 306–321.
12 Z. Fang, C. Ye, T. Ling, H. Ji, C. Lu, C. Ke, X. Zhuang and J. Shan, *Chem Catal.*, 2024, **4**, 101145.
13 R. Yanagi, P. Yang, A. W. Tricker, Y. Chen, M. C. Scott, S. A. Berlinger, I. V. Zenyuk and X. Peng, *Joule*, 2025, **9**, 102001.
14 Y. Kang, Y. Tang, L. Zhu, B. Jiang, X. Xu, O. Guselnikova, H. Li, T. Asahi and Y. Yamauchi, *ACS Catal.*, 2022, **12**, 14773–14793.
15 R. Sun, X. Huang, J. Jiang, W. Xu, S. Zhou, Y. Wei, M. Li, Y. Chen and S. Han, *Dalton Trans.*, 2022, **51**, 15205–15226.
16 Y. Chen, Q. Li, Y. Lin, J. Liu, J. Pan, J. Hu and X. Xu, *Nat. Commun.*, 2024, **15**, 7278.
17 H. Yang, M. Driess and P. W. Menezes, *Adv. Energy Mater.*, 2021, **11**, 2102074.
18 S. Gupta, M. K. Patel, A. Miotello and N. Patel, *Adv. Funct. Mater.*, 2020, **30**, 1906481.
19 E. Lee and B. P. T. Fokwa, *Acc. Chem. Res.*, 2022, **55**, 56–64.
20 J. Hong, S. Mutalik, P. P. Pescarmona and L. Protesescu, *Chem. Mater.*, 2024, **36**, 2147–2164.
21 E. Sadeghi, S. Chamani, N. S. Peighambardoust and U. Aydemir, *Energy Environ. Mater.*, 2025, **8**, e12873.
22 J. Masa, P. Weide, D. Peeters, I. Sinev, W. Xia, Z. Sun, C. Somsen, M. Muhler and W. Schuhmann, *Adv. Energy Mater.*, 2016, **6**, 1502313.
23 B. Xu, B. Chong, H. Li and G. Yang, *Chem. Eng. Sci.*, 2023, **280**, 118985.
24 S. Gupta, R. Fernandes, R. Patel, M. Spreitzer and N. Patel, *Appl. Catal., A*, 2023, **661**, 119254.
25 D. Zhu, L. Wang, M. Qiao and J. Liu, *Chem. Commun.*, 2020, **56**, 7159–7162.
26 Y. Chen, Z. Lai, X. Zhang, Z. Fan, Q. He, C. Tan and H. Zhang, *Nat. Rev. Chem.*, 2020, **4**, 243–256.
27 M. Singh, D. C. Cha, T. I. Singh, A. Maibam, D. R. Paudel, D. H. Nam, T. H. Kim, S. Yoo and S. Lee, *Mater. Chem. Front.*, 2023, **7**, 6254–6280.
28 Y. Liu, Q. Li, R. Si, G.-D. Li, W. Li, D.-P. Liu, D. Wang, L. Sun, Y. Zhang and X. Zou, *Adv. Mater.*, 2017, **29**, 1606200.
29 Y. Chen, C. Liu, J. Xu, C. Xia, P. Wang, B. Y. Xia, Y. Yan and X. Wang, *Small Struct.*, 2023, **4**, 2200130.
30 H. Lan, J. Wang, L. Cheng, D. Yu, H. Wang and L. Guo, *Chem. Soc. Rev.*, 2024, **53**, 684–713.
31 S. Carenco, D. Portehault, C. Boissière, N. Mézailles and C. Sanchez, *Chem. Rev.*, 2013, **113**, 7981–8065.
32 J. M. V. Nsanzimana, L. Gong, R. Dangol, V. Reddu, V. Jose, B. Y. Xia, Q. Yan, J.-M. Lee and X. Wang, *Adv. Energy Mater.*, 2019, **9**, 1901503.
33 B. Albert and K. Hofmann, *Handbook of Solid State Chemistry*, 2017, pp. 435–453, DOI: 10.1002/9783527691036.hsscvol1011.
34 M. Lewandowski, M. Bartoszewicz, K. Jaroszewska and G. Djéga-Mariadassou, *J. Ind. Eng. Chem.*, 2022, **116**, 75–98.
35 H. Sun, J. Meng, L. Jiao, F. Cheng and J. Chen, *Inorg. Chem. Front.*, 2018, **5**, 760–772.
36 Y. Qi, Y. Zhang, L. Yang, Y. Zhao, Y. Zhu, H. Jiang and C. Li, *Nat. Commun.*, 2022, **13**, 4602.
37 Q. Yun, Y. Ge, Z. Shi, J. Liu, X. Wang, A. Zhang, B. Huang, Y. Yao, Q. Luo, L. Zhai, J. Ge, Y. Peng, C. Gong, M. Zhao, Y. Qin, C. Ma, G. Wang, Q. Wa, X. Zhou, Z. Li, S. Li, W. Zhai, H. Yang, Y. Ren, Y. Wang, L. Li, X. Ruan, Y. Wu, B. Chen, Q. Lu, Z. Lai, Q. He, X. Huang, Y. Chen and H. Zhang, *Chem. Rev.*, 2023, **123**, 13489–13692.
38 X. Wang, Y. V. Kolen'ko, X.-Q. Bao, K. Kovnir and L. Liu, *Angew. Chem., Int. Ed.*, 2015, **54**, 8188–8192.
39 N. Patel and A. Miotello, *Int. J. Hydrogen Energy*, 2015, **40**, 1429–1464.
40 M. C. Biesinger, B. P. Payne, A. P. Grosvenor, L. W. M. Lau, A. R. Gerson and R. S. C. Smart, *Appl. Surf. Sci.*, 2011, **257**, 2717–2730.
41 V. Jose, J. M. V. Nsanzimana, H. Hu, J. Choi, X. Wang and J.-M. Lee, *Adv. Energy Mater.*, 2021, **11**, 2100157.
42 Y. Zou, Y. Gao, P. Huang, C. Xiang, H. Chu, S. Qiu, E. Yan, F. Xu and L. Sun, *Metals*, 2017, **7**, 365.
43 P. W. Menezes, C. Panda, S. Loos, F. Bunschei-Bruns, C. Walter, M. Schwarze, X. Deng, H. Dau and M. Driess, *Energy Environ. Sci.*, 2018, **11**, 1287–1298.
44 Y. Liu, J. Zhang, X. Li, Z. Zeng, X. Cheng, Y. Wang and M. Pan, *Int. J. Electrochem. Sci.*, 2019, **14**, 6123–6132.
45 Y. Tian, X. Lian, Y. Wu, W. Guo and S. Wang, *CrystEngComm*, 2020, **22**, 5218–5225.
46 H. Pang, C. Wei, Y. Ma, S. Zhao, G. Li, J. Zhang, J. Chen and S. Li, *ChemPlusChem*, 2013, **78**, 546–553.
47 A. Chunduri, S. Gupta, O. Bapat, A. Bhide, R. Fernandes, M. K. Patel, V. Bambole, A. Miotello and N. Patel, *Appl. Catal., B*, 2019, **259**, 118051.
48 G. Gouget, D. P. Debecker, A. Kim, G. Olivieri, J.-J. Gallet, F. Bournel, C. Thomas, O. Ersen, S. Moldovan, C. Sanchez, S. Carenco and D. Portehault, *Inorg. Chem.*, 2017, **56**, 9225–9234.
49 Z. Wang, X. Ke and M. Sui, *Front. Chem.*, 2022, **10**, 872117.
50 H. Tan, J. Verbeeck, A. Abakumov and G. Van Tendeloo, *Ultramicroscopy*, 2012, **116**, 24–33.
51 J. Kundu, H. J. Kim, M. Li, H. Huang and S.-I. Choi, *Mater. Chem. Front.*, 2023, **7**, 6366–6388.
52 N. Mahmood, Y. Yao, J.-W. Zhang, L. Pan, X. Zhang and J.-J. Zou, *Adv. Sci.*, 2018, **5**, 1700464.
53 J. M. V. Nsanzimana, L. Cai, D. Abdoulaye, G. Pagot, P. Mattana, K. Vezzù, E. Negro, B. Y. Xia and V. Di Noto, *Adv. Energy Mater.*, 2025, **15**, 2501686.

54 Q. Cai, W. Hong, C. Jian, X. He and W. Liu, *Adv. Energy Sustainability Res.*, 2023, **4**, 2200178.
55 H. Sun, Z. Yan, F. Liu, W. Xu, F. Cheng and J. Chen, *Adv. Mater.*, 2020, **32**, 1806326.
56 X. Shi, W. Gu, B. Zhang, Y. Zhao, A. Zhang, W. Xiao, S. Wei and H. Pang, *Adv. Funct. Mater.*, 2025, **35**, 2423760.
57 G. Kresse and J. Furthmüller, *Comput. Mater. Sci.*, 1996, **6**, 15–50.
58 E. E. Siddharthan, S. Ghosh and R. Thapa, *ACS Appl. Energy Mater.*, 2023, **6**, 8941–8948.
59 Y. He, Z. Ma, F. Yan, C. Zhu, T. Shen, S. Chou, X. Zhang and Y. Chen, *Proc. Natl. Acad. Sci. U. S. A.*, 2024, **121**, e2320777121.